This is the Pre-Published Version.

The following publication Li, Y., Wu, X., Ho, W., Lv, K., Li, Q., Li, M., & Lee, S. C. (2018). Graphene-induced formation of visible-light-responsive SnO2-Zn2SnO4 Z-scheme photocatalyst with surface vacancy for the enhanced photoreactivity towards NO and acetone oxidation. Chemical Engineering Journal, 336, 200-210 is available at https://doi.org/10.1016/j.cej.2017.11.045.

Graphene-Induced Surface Vacancy of Zn_2SnO_4 for the Enhanced Visible-Light-Driven Photocatalytic Oxidation of NO and Acetone

Yuhan Li[a,b,c], Xiaofang Wu[b], Wingkei Ho[a,*], Kangle Lv[b,*], Qin Li[b], Mei Li[b], Shun Cheng Lee[d]

[a]Department of Science and Environmental Studies, The Education University of Hong Kong, Tai Po, N.T., Hong Kong, P.R. China

[b]Key Laboratory of Catalysis and Materials Science of the State Ethnic Affairs Commission and Ministry of Education, Hubei Province, College of Resources and Environmental Science, South-Central University for Nationalities, Wuhan 430074, P.R. China

[c]Engineering Research Center for Waste Oil Recovery Technology and Equipment, Ministry of Education, Chongqing Key Laboratory of Catalysis and New Environmental Materials, Chongqing Technology and Business University, Chongqing 400067, P.R. China.

[d]Department of Civil and Environmental Engineering, The Hong Kong Polytechnic University, Hung Hom, Hong Kong, P.R. China

Tel.: +852-2948 8255; Fax: +852-2948 7726.

E-mail: lvkangle@mail.scuec.edu.cn (K.L. Lv)

E-mail: keithho@ied.edu.hk (W.K. Ho)

© 2017. This manuscript version is made available under the CC-BY-NC-ND 4.0 license http://creativecommons.org/licenses/by-nc-nd/4.0/

Abstract

As a ternary complex oxide with good physic-chemical stability, Zn_2SnO_4 is a promising candidate in the photocatalytic application. However, the photocatalytic activity of Zn_2SnO_4 needs further to improve due to its wide bandgap (about 3.4 eV) and intrinsic high recombination rate of photo-generated charge carriers. In this paper, the positive influence of graphene on the structure and visible photocatalytic activity of Zn_2SnO_4 in oxidation of NO and acetone was systematically investigated based on the fact that graphene has the property of high electronic conductivity for transporting and storing electrons. It was found that the presence of graphene not only induces the formation of SnO_2, but also introduces Sn vacancy, which can trigger the visible light photocatalytic activity. The photocatalyst loaded with 3.0 wt.% of graphene shows the highest photocatalytic reactivity in oxidation of NO and acetone under visible light illumination. Graphene can efficiently transfer the photo-produced electrons from the conduction band of Zn_2SnO_4, retarding the recombination of carriers and therefore enhancing the visible photo-reactivity. A visible-light-responsive photocatalytic reaction model based on the three-component-photocatalyst SnO_2/Zn_2SnO_4/graphene was put forward.

Keywords: Zn_2SnO_4; Graphene; Photocatalytic oxidation; NO; Acetone.

1. Introduction.

Nitrogen oxides (NO_x), generally produced from the fossil fuels incineration and vehicle exhaust emission, are universally acknowledged as pollutants in air, owing to the fact that this kind of contaminant can bring about various atmospheric environmental pollutions such as haze, acid rain and photochemical smog[1]. There are traditional strategies such as selective catalytic reduction (SCR), thermal catalysis, and adsorption that can be used for controlling the NO_x pollution from industrial emission, however, it is a big challenge to eliminate indoor air NO_x with low concentration of ppb (parts per billion) level [2]. As one of hazardous volatile organic compounds (VOCs), acetone is also rich in indoor environment. It has been reported that high exposure to acetone vapor (up to 500 ppm) can incur irritation in eyes and respiratory system [3]. Additionally, accidental intake of large amounts of acetone can cause unconsciousness and death [4]. Therefore, it is substantially important to search an efficient technology to purify these two typical air pollutants. Photocatalysis, as an effective and environmentally benign technology, is extremely promising for purifying polluted air under mild conditions [5-8].

Zn_2SnO_4, as a ternary complex oxide zinc stannate with high electrical conductivity, fast electron diffusivity, good physic-chemical stability, is a significant n-type semiconducting oxide and a promising candidate in the photocatalytic application [9, 10]. However, the photocatalytic activity of Zn_2SnO_4 is not high enough to satify the practical applications not only because it can only be excited by UV light due to its wide bandgap (around 3.4 eV) [11], but also due to its high intrinsic recombination rate of photo-produced carriers[12]. Hence, tremendous attention have been attracted to tailor the band structure of Zn_2SnO_4, endowing it responsive to visible light[13, 14]. However, it still remains a great challenge.

Recently, some groups have reported non-stoichiometric semiconductor-based photocatalysts such as vacancy-rich ZnO_{1-x}[15], SnO_{2-x}[16], and TiO_{2-x}[13] nanostructures, which performed improved photocatalytic performance. The distortion of crystal lattice can introduce a proper platform for retarding the photo-induced electron-hole recombination, leading to enhanced photocatalytic efficiency and stability when illuminating with visible light[15].

In recent years, the study of graphene, a two dimensional (2D) material, has attracted much attention due to its excellent mobility of charge carriers, large specific surface area, flexible structure, and good electrical and thermal conductivity[17-19]. Graphene has been often used for decoration/modification of semiconductor photocatalysts such as TiO_2 [20], Bi_2WO_6 [21] and CdS[22] because it can efficient reduce the recombination rate of photo-generated electron-hole pairs when coupling with semiconductors, thereby increasing the photocatalytic performances.

In this paper, a visible-light-resposive three-component all solid SnO_2-Zn_2SnO_4/graphene Z-scheme photocatalyst was prepared by a facile one-pot hydrothermal methods. In this high efficient Z-scheme photocatalyst, a host of vacancies were introduced to trigger the wide-bandgap of SnO_2 and Zn_2SnO_4 that can be sensitive to visible light, and reduced graphene oxide (rGO) performed as an effective electron mediator. To the best of our knowledge, this is the first time to report the fabrication of vacancy-rich SnO_2-Zn_2SnO_4/graphene Z-scheme photocatalyst, which shows high visible light photocatalytic activity in degradation/minerization of NO and acetone in air.

2. Experimental

2.1 Preparation of SnO_2/Zn_2SnO_4/graphene composite.

All the chemicals with analytical grade were directly used in this study (Sigma Aldrich). The water used in this research was deionized by Nano pure filtration systems to the standard resistivity of 18 MΩ·cm. The typical fabrication process of Zn_2SnO_4 octahedrons is as follows. Firstly, 1.96 mmol of L-tryptophan were dissolved in 25 mL of H_2O. Then 1.18 mmol of $Zn(CH_3COO)_2·2H_2O$ and 0.75 mmol of $SnCl_4·4H_2O$ were added to the above solution with strong stir at 60 °C. After stirring for 30 min, 5 mL of NaOH aqueous solution (1.45 $molL^{-1}$) was dropwise added to the mixed solution, and the resulted mixture was marked as solution A. Simultaneously, certain amount (0.00167 g, 0.0050 g and 0.00835 g) of graphene nanoplatelets (International Laboratory USA, 6-8 nm thick × 25 microns wide) were ultrasonicated for 60 min to obtained a well dispersed solution, which was marked as solution B. Afterwards, solution B was dropwise added to solution A under vigorously stirring. After stirring for 60 min, the slurry was transferred to a stainless 100 mL Teflon-lined autoclave, which was then hydrothermally treated at 200 °C for 24 h. Finally, the obtained grey precipitates after centrifugation were washed with deionized water and absolute ethanol for three times. The nominal mass ratios of graphene to Zn_2SnO_4 were controlled at 1.0, 3.0, and 5.0%, and the corresponding Zn_2SnO_4/graphene photocatalysts were labelled as ZL-G1, ZL-G3 and ZL-G5, respectively. For comparison, we also prepared individual Zn_2SnO_4 octahedrons under other identical conditions but in the absence of graphene, which were simply marked as ZL.

2.2 Characterization

X-ray diffractometer (XRD; D/max RA, Japan) was applied to investigate the crystalline phase structures of the as-obtained photocatalysts. Scanning electron microscope (SEM; JEOL JSM-6490, Japan) and transmission electron microscopy

(TEM; JEM-2010, Japan) were used to observe the morphological features and microstructures of the as-synthesized samples. Nitrogen adsorption-desorption isotherms were attained from a nitrogen adsorption equipment (ASAP 2020, USA), from which all the photocatalysts were degassed firstly at 150 °C and followed by investigating the surface areas and pore size distribution of the photocatalysts. FT-IR spectroscopy in a Nicolet Nexus spectrometer can be used for studying the functional groups on the sample surface by wrapping the photocatalysts in KBr pellets. X-ray photoelectron spectroscopy (XPS) with Al Kα X-ray (hv = 1486.6 eV) operated at 150 W (Thermo ESCALAB 250, USA) can be used for investigating the surface chemical composition and the total density of state (DOS) distribution in the valence band (VB). As an internal standard, the C 1*s* centered at 284.8 eV can be used for correcting the skewing of the binding energy because of correlative surface charging. Scan UV-Vis spectrophotometer (UV-Vis DRS; UV-2450, Shimadzu, Japan) configured with an integrating sphere assembly by employing $BaSO_4$ as the reflectance specimen can be used for gaining the optical properties of the samples. Fluorescence spectrophotometer (FS-2500, Japan) with a Xe lamp and an optical filter as a stimulation source can be utilized to get the information of photoluminescence spectra (abbreviated to: PL) of the photocatalysts. Fluorescence spectrophotometer (Edinburgh Instruments, FLSP-920) can be applied to obtain the steady and time-resolved fluorescence emission spectra of as-prepared samples. Electron paramagnetic resonance (EPR) spectra were conducted on a Bruker EMX EPR spectrometer (Billerica, MA).

In a three-electrode system, the photocurrent of photocatalysts were measured with a electrochemical workstation (CHI 760E, Shanghai). The as-prepared samples were used as working electrode, Ag/AgCl and Pt wire were used as reference and counter electrode, respectively. Aqueous Na_2SO_4 (0.5 M) was used as electrolyte solution. A 3 W LED lamp emitted mainly at λ=420±10 nm was used as the light source. The working electrode was obtained by doctor-blade approach *via* using ITO glass (1cm×1cm) as substrate. The spreading slurries of as-obtained photocatalyst were fabricated by grinding the mixture containing 50 mg of samples, 30 mg of polyethene glycol (MW: 20000) and 800 uL of deionized water. Afterwards, the film was annealed at 250 ºC for 30 min. Electrochemical impedance researches of as-prepared samples were also performed at the open-circuit potential. An ac disturbance of 5 mV was applied to the working electrode on the frequency in the range of 0.1 Hz to 1000Hz.

Electron spin resonance (ESR) signals of radicals spin-trapped by 5,5-dimethyl-1-pyrroline N-oxide (DMPO) were recorded on a spectrometer (JES FA200). Specimens for ESR measurement were obtained by mixing the photocatalysts in a 40 mM DMPO solution tank (methanol dispersion for DMPO-$O_2•^-$ and aqueous dispersion for DMPO-•OH) and illuminated with visible light (λ> 400 nm).

2.3 Visible light photocatalytic oxidation of NO.

In a consecutive flow reactor, the photo-oxidation reactivity of the as-obtained products was tested in terms of the ppb level oxidation of NO at ambient temperature. The volume of the rectangular reactor constituted stainless steel with quartz glass as cover was 4.5 L (*L*×*W*×*H,* 30.0 cm×15.0 cm×10.0 cm). Simulated visible light source was acquired from an LED lamp (λ> 400 nm). There with 30 mL of deionized water was poured into 0.2 g of the as-obtained samples, the mixed solution was subjected to ultra-sonicate for 30 min. The resulting suspension was sedimentated onto a culture dish with a diameter of 11.5 cm. The dish with sample was heated at 60 °C for 3 h to thoroughly evaporate water and then cooled down to normal temperature. NO gas was supplied from a compressed gas cylinder having 50 ppm of NO (N_2 balance) in line with traceable standards recommended by the National Institute of Stands and Technology. An air stream produced by a zero-air generator (Advanced Pollution Instrumentation, A Teledyne Technologies Co., Model 701) can be used for diluting the initial NO concentration to about 600 ppb. In a gas blender, the gas streams were totally premixed, the gas flow rate was setting as 1.0 $L \cdot min^{-1}$ by employing a mass flow controller. When the gas system can reach adsorption-desorption balance, turning on the lamp. A chemiluminescence NO_x analyzer (Advanced Pollution Instrumentation, A Teledyne Technologies Co., Model T200) can be used for monitoring the concentrations of NO, NO_2 and NO_x (NO_x=NO+NO_2) continuously, at a gas flow rate of 1.0 $L \cdot min^{-1}$. The formula η (%) = $(1 - C/C_0) \times 100\%$ was used to calculate the removal ratio (η) of NO accordingly, where C_0 and C are the initial feeding gas stream and the NO concentration in the outlet steam, respectively.

2.4 Visible light photocatalytic degradation of acetone.

The photo-decomposition of acetone was measured under visible light illumination ($\lambda > 400$ nm) at 25 ºC by adopting a 15 L reactor. 0.3 g of aqueous Zn_2SnO_4 suspension was coating onto three cultrue dishes with diameter of 7.0 cm. The dishes coated with Zn_2SnO_4 were dried in an oven at 80 ºC for 2 h and then placed in the reactor. Afterwards, 10 μL of acetone was injected into the reactor by using a microsyringe. The concentrations of carbon dioxide and acetone in the reactor can be mointorred on line with a Photoacoustic IR Multigas Monitor (INNOVA Air Tech Instruments, Model 1412). After the adsorption equilibrium, the initial concentration of acetone can reach 300 ppm, which can maintain constant for around 35 min until turning on a visible light LED lamp ($\lambda > 400$ nm). Each set of experiment was followed for 140 min.

3. Results and discussion

3.1 XRD patterns and microstructures

Powder XRD measurements were performed to confirm the crystal phase of the photocatalysts and ascertain the effect of graphene on the phase and crystallinity. As shown in Fig. 1, ZL sample (Fig. 1a) exhibits the representative diffraction peaks of Zn_2SnO_4 (JCPDS#24-1470)[9] without any other impurity peaks. After introducing a small amount of graphene, however, there is a distinct phase transformation from pure Zn_2SnO_4 to a mixed Zn_2SnO_4 and rutile-SnO_2 (JCPDS#41-1445)[12]. When further increase in the amount of graphene, the diffraction peak intensities of SnO_2 steady increase. No characteristic diffraction peaks for graphene are detected, possibly due to its limited content and relatively low crystallinity[18]. Such features can, undoubtedly, demonstrate that there exists a significant influence of the interference of graphene on crystal phase and crystallinity of Zn_2SnO_4. As reported previously, Zn_2SnO_4-SnO_2 composites can be obtained by re-heating $ZnSn(OH)_6$ at high temperature (> 800 °C) for a long time (> 6h) [12, 23]. In our system, however, Zn_2SnO_4-SnO_2 composites was successfully fabricated by a facile one-pot hydrothermal strategy with the help of only a small amount of graphene.

The over all reaction on the formation of Zn_2SnO_4 in solution is as follow (eq. 1) [24]:

$$2Zn^{2+} + Sn^{4+} + 8OH^- \rightarrow Zn_2SnO_4(s) + H_2O \qquad (1)$$

Different from in homogeneous solution, after addition of graphene, positively charged Sn^{4+} prefers to adsorb on the surface of electron-rich graphene. This is because the ionic radius of Sn^{4+} is close to that of Zn^{2+} (0.74 A°)[25]. However, Sn^{4+}

has more positive charges than Zn^{2+}. During hydrothermal reaction, SnO_2 is therefore produced due to the hydrolysis of the high concentrated Sn^{4+} adsorbed on the surface of graphene (eq. 2).

$$Sn^{4+} + 4OH^{-} \rightarrow SnO_2(s) + H_2O \qquad (2)$$

Therefore, the presence of graphene facilitates the formation of SnO_2 during the preparation of Zn_2SnO_4.

The influence of graphene on the morphological structure of the as-obtained photocatalyst was explored by SEM (Fig. 2) . From Fig. 2a, it can be seen that pristine Zn_2SnO_4 particles (ZL sample) exhibit octahedral shape with a sidelength of 0.5-0.8 um. Zn_2SnO_4 nanoparticles usually form in shapes of octahedrons [25, 26] and cubes [27], depending on the solution pH, reaction temperature and capping reagent during hdyrothermal reaction[28]. After introducing 1.0 wt.% of graphene, highly aggregated octahedrons with sidelengths of 0.3-0.5 um are found to anchor on the surface of exfoliated graphene (Fig. 2b). This phenomenon gives direct evidence that the introduction of graphene can cause a smaller particle size of Zn_2SnO_4, consistent with the XRD analytical results (Fig. 1). This is because graphene can act as nucleation centers during the hydrothermal reaction, which makes an easy nucleation and therefore prevents the overgrowth of Zn_2SnO_4 polyhedrons in solution. With increase in the amount of graphene to 3.0 wt.% and 5.0 wt.%, the aggregation of Zn_2SnO_4 particles was efficiently prevented, and most of the particles were found to be wraped by graphene films (Fig. 2c and 2d).

Fig. 3a shows the TEM image of sheet-like graphene, reflecting its successful exfoliation. The polyhedral structures of Zn_2SnO_4 was further confirmed by their solid centers (Fig. 3b). From the TEM image of ZL-G3 sample (Fig. 3c and 3d), it can be seen that Zn_2SnO_4 polyhydrons are strongly anchored on the surface of graphene films. The strong interaction between graphene and Zn_2SnO_4 can faciliate the electron transferring from the conduction band (CB) of Zn_2SnO_4 to graphene, enhancing the photocatalytic activity of Zn_2SnO_4. The strong interaction between graphene and Zn_2SnO_4 was further confirmed by XPS characterization result, which will be shown below.

3.2. FTIR and XPS analysis

To disclose the chemical states of these specimens and further determine the presence of graphene in the composites, the FTIR were examined. As we can see from Fig. S1, the absorption bands located at 584.9, 1076.9 and 1627.0 cm^{-1} are ascribed to the vibration of M-O or M-O-M (M stands for Sn or Zn) functional groups in SnO_2 and Zn_2SnO_4 [29]. The obvious broad bands at 3427.4 cm^{-1} can be indexed to the stretching vibration of H_2O molecules.

XPS spectra were further used to study the surface chemical states of Zn_2SnO_4-SnO_2/graphene composite. As displayed in Fig. 4, the XPS survey spectra reveal the existence of Zn, Sn, O elements and a trace amount of C in the samples. When compared with that of ZL sample (Fig. 4a), the signal of C1s peak for ZL-G3 sample (Fig. 4b) is much stronger, confirming the successful introduction of graphene into ZL-G3 sample.

In high-resolution XPS spectra of Zn 2*p* (Fig. 5A), for ZL sample, two prominent peaks with binding energies of 1021.8 and 1044.9 eV can be observed, which are assigned to the signals of $2p_{3/2}$ and $2p_{1/2}$ of Zn^{2+} ion[30], respectively. However, for ZL-G3 sample, the binding energies of Zn $2p_{3/2}$ and $2p_{1/2}$ shift to higher binding energies of 1022.4 eV and 1045.5 eV, both increased about 0.6 eV. The increased binding energy indicates a reduced electron density, which could be ascribed to two possibilities: (i) electron of Zn_2SnO_4-SnO_2 transfer to graphene; (ii) the existence of defects.

Fig. 5B presents the high resolution XPS spectra of Sn 3*d* main peak at 486.5 eV (Sn $3d_{5/2}$) with a satellite peak at 494.9 eV (Sn $3d_{3/2}$) [31] for ZL sample. After incorporation of graphene (3 wt.%, that is, 0.005 g), however, the Sn 3*d* peak of ZL-G3 shifts upwards by 1.0 eV. Moreover, the intensity of two peaks on ZL-G3 was remarkably populated when compared with that of ZL sample. The upward shifts and enhanced intensity can be indicative of the formation of SnO_2 resulted from the charge reassignment, while, potentially reflecting a certain concentration of Sn defects in ZL-G3 sample.

In O 1s high-resolution XPS spectra (Fig. 5C), a well-formed peak emerging at 530.4 eV and one shoulder appearing at 532.2 eV can be observed for ZL and ZL-G3 samples. The peak at 532.2 eV is assigned to surface O species like the coordination of O in Sn-O-Zn or -OH in water, while the other one centering at 530.4 eV is ascribed to the lattice O in Sn-O-Sn[11]. Additionally, the similar intensity and peak shape as well the same separation between the main and shoulder peaks strongly reveal that there does not exist any change in the surface chemical status of O atoms.

For the bare graphene in ZL-G3 sample, the C 1s XPS spectrum (Fig. 5D) exhibits the luxuriant oxygen-containing functional bondings on the surface of ZL-G3, which proves the oxidation of graphene to graphene oxide to some extent. The partially oxygenated graphene further confirms the strong interaction between graphene and Zn_2SnO_4-SnO_2 composites, consistent with the SEM (Fig. 2) and TEM (Fig. 3) characterization results.

On the basis of the above discussions, together with features of peak shifts, therefore, EPR was exerted to confirm the potential presence of defects in the as-obtained samples. As can be seen from Fig. 6, for ZL sample, no EPR signals can be witnessed. Unsurprisingly, after the introduction of graphene, all three Zn_2SnO_4 samples display an evident EPR resonance signal at $g \approx 1.87$, which can be assigned to Sn defects[32]. Furthermore, the intensity of the EPR signal increases with increase in the content of graphene, indicating that the introduction of graphene does disturb the hydrothermal reaction process of the precursors. Actually, Georgakilas *et al.* found that graphene nanosheets can function an actuator to lower energies by interactions of charge-transfer or π-π*[33]. Zhang *et al.* overthrowed the traditional role of graphene as electron reservoir and, therefore, found it can work as a macromolecular photosensitizer to transmute wide band gap ZnS into a visible light material[34]. Nevertheless, to our best knowledge, it has not been reported that introducing the graphene can induce the formation of defects, and the concentration of defects can be tailored by simply control the amount of graphene. However, high concentrated defects may act as the recombination centers, detrimental to the photocatalytic activity of the photocatalyst.

3.3 Visible light photo-oxidation of NO.

To study the effect of defects on the photocatalytic performance of graphene modified Zn_2SnO_4 samples (ZL-G), visible photocatalytic oxidation of NO in ppb level was performed using ZL alone and ZL-G composite as photocatalyst (Fig. 5A), respectively. NO is robust and cannot be photo-oxidized under visible light irradiation without photocatalyst (not shown here). It can be clearly seen that, ZL alone offers negligible visible light photo-oxidation perforamance for NO removal. Surprisingly, the NO removal ratio of ZL-G1, ZL-G3 and ZL-G5 three samples are increased to 41.5%, 59.3%, and 32.6%, respectively (Fig. 7A), much higher than that of ZL sample (only 7.5%).

We also online observed the produced NO_2 concentration profiles as irradiation time (Fig.7B), and found that the instantaneous concentration of NO_2 shows a similar trend in terms of the corresponding NO removal. The photocatalytic performance of ZL-G hybrids can be adjusted by optimizing the weight ratio of graphene to Zn_2SnO_4-SnO_2. Inferior photo-oxidation rate of NO are obtained by ZL-G1 and ZL-G5 samples with too small or too much graphene. This result can origin from the fact that, graphene by itself could not straightforwardly exert as visible light material for photo-oxidation of NO due to its zero band gap[34], and thereby, its excess existence in ZL-G composites may block physically from Zn_2SnO_4-SnO_2 harvesting light. Remarkably, the superior photocatalytic NO removal ratio of ZL-G photocatalysts still even outperforms that of other categories of decent visible-light-triggered photocatalytic materials such as BiOBr (21.3%)[35], BiOI (14.9%)[36] and g-C_3N_4 (12.5%)[37]. In the absence of graphene, however, the Zn_2SnO_4-SnO_2 composite shows poor photoreactivity in degradation of MB dye even under the UV irradiation[27]. This work is different from the pioneering studies on semiconductors modified with cabon materials such as carbon nanotubes, C_{60} and graphene), where carbon materials mainly act as electron sinks. In the present study, however, we found that graphene can introduce the defects and exert as a possible visible light photosensitizer, which therefore endows ZL-G photocatalyst with visible photocatalytic activity.

3.4 Photo-oxidation of acetone under visible light illumination.

As a typical contaminant of volatile organic compounds (VOCs), acetone in air can cause nervous system disorders. Therefore, we chose acetone as a target pollutant and photocatalytical degradation of acetone in ppm level was performed under the visible light irradiation. Zn_2SnO_4 and SnO_2 are usually deemed to be hardly responsive photocatalysts for decomposing acetone under visible light illumination because of their wide bang gap. However, in Fig. 8, it was found that the concentration of acetone gradually declines and the amount of released CO_2 accumulates under visible light illumination. Particularly, the content of CO_2 formation for ZL-G3 sample can reach around 80 ppm within 140 min. All these results manifest that ZL-G3 could function as a high efficient visible-light-responsive photocatalytic material for both NO and acetone oxidation. As far as we know, this is the first example to manifest SnO_2-Zn_2SnO_4/graphene with visible light photoreactivity.

3.5 Optical property.

The above-described results afforded solid evidence that ZL-G photocatalysts can offer eminent photocatalytic performance under visible light irradiation. To account for the visible light photoreactivity of ZL-G photocatalyst, the UV-vis DRS and PL spectra were investigated (Fig. 9). Although all the samples show strong absorption in the UV region (Fig. 9A), an obvious increase in the visible range from 400 to 800 nm was observed after the addition of graphene. With increasing the content of graphene, the color of the photocatalyst changes from white (ZL) to darkgray (ZL-G3), indicating an enhanced light-harvesting ability in visible region. As reported by Zhang *et al.*, graphene materials can trigger a remarkably strong surface plasmon absorption even in the near-infrared region[38]. Thus, it is understandable that the presence of graphene can significantly affect the optical property of Zn_2SnO_4-SnO_2 composite. Meanwhile, as can be seen from Fig. 9B, ZL displays the strongest PL emission in visible region, reflecting the quick recombination rate of photo-produced carriers. The PL peaks for ZL-G composites are much smaller when compared with that of ZL sample. Therefore, we can understand the graphene-induced efficient transportation and separation of carriers.

3.6 Photocurrent and electrochemical impedance study.

To further validate the contribution of graphene to the charge carriers separation efficiency of Zn_2SnO_4-SnO_2/graphene composites, the transient photocurrent test over five consecutive on/off cycles was performed under visible light illumination (λ>400 nm) and was displayed in Fig. 10A. As can be seen that ZL-G3 possesses the highest photocurrent among all the photocatalysts, indicating it has the fastest charge separation efficiency and longest charge carriers lifetime. Additionally, Fig. 10C illustrates the interfacial charge transfer ability for the obtained photocatalysts by EIS measurements. Obviously, ZL-G3 sample has the smallest semicircle radius, also showing a smallest charge transfer resistance and highest interfacial charge carriers transfer efficiency[8]. Therefore, it is safe to believe that the existence of appropriate graphene in hybrids can expedite the transfer and separation of photo-generated carriers.

3.7 BET surface areas and pore structure.

Xiong *et al*. reported that[39], wide band gap semiconductor $(BiO)_2CO_3$ with hierarchical microspheres showed outstanding visible-light-responsive photocatalytic activity due to the strong visible light reflecting and scattering effects. Triggered by this report, to ascertain the possible contribution of specific surface areas and pore volume to photocatalysis process, nitrogen adsorption-desorption isotherms were analyzed (Fig. 11). It can be seen that all photocatalysts show similar adsorption-desorption isotherms and pore structures. The BET surface area of the photocatalyst slightly but steadily increases from 21.3 to 24.3 m^2g^{-1} with increasing in the amount of graphene (Table 1). Enlarged BET surface area means more active site can be used for the adsorption and reaction for photocatalytic degradation, enhancing the photoreactivity.

3.8 Active species for photocatalytic oxidation of NO.

It was reported that, NO can be removed *via* photocatalytic oxidation processe due to the continuous attacks of reactive oxygen species (ROSs) such as $\cdot O_2^-$ and $\cdot OH$ radicals. To shed light on the effect of graphene on the enhanced photoreactivity of SnO_2-Zn_2SnO_4/graphene composite, ESR measurement was used to monitor the possible ROSs[40]. As can be seen from Fig. S2 that, for ZL sample, no obvious ESR signal can be detected in the dark or under visible light irradiation. While, for ZL-G3 sample, distinct peaks for DMPO-$\cdot O_2^-$ (Fig. 12 A) and DMPO-$\cdot OH$ (Fig. 12B) adduct signals are observed under visible light illumination. Both of the peak intensities for DMPO-$\cdot OH$ and DMPO-$\cdot O_2^-$ radicals steadily increase as irradiation time, which begin to decrease when the light is turned off. These results firmly demonstrates that $\cdot O_2^-$ and $\cdot OH$ radicals are main ROSs that should be responsible for the effective photo-oxidation of NO (eqs. 5-8) and acetone (eq. 9) [41, 42].

$$NO + \cdot O_2^- \rightarrow NO_3^- \quad (5)$$

$$NO + 2\cdot OH \rightarrow NO_2 + H_2O \quad (6)$$

$$NO_2 + \cdot OH \rightarrow NO_3^- + H^+ \quad (7)$$

$$NO + NO_2 + H_2O \rightarrow 2HNO_2 \quad (8)$$

$$C_3H_6O + \cdot O_2^-/\cdot OH \rightarrow CO_2 + H_2O \quad (9)$$

3.9 Proposed photocatalytic reaction mechanism.

From the viewpoint of kinetic and thermodynamic requirements for photo-oxidation of NO and acetone, it is then necessary to estimate band edge positions according to the formula of Mulliken assumption[43]. The CB value of as-obtained photocatalysts can be calculated by the formula: $E_{CB}=X-E^C-1/2E_g$, where X stands for the Mulliken electronegativity of the photocatalyst, E^C represents the energy of free lectrons on the hydrogen level (around 4.5 eV) and E_g is the forbidden gap energy. The calculated CB minimum of Zn_2SnO_4 and SnO_2 are -0.22

and 0.05 eV, and the VB maximum of Zn_2SnO_4 and SnO_2 are 3.18 and 3.25 eV, respectively.

In principle, Zn_2SnO_4 and SnO_2 can not be excited to produce ROSs such as $^{\bullet}O_2^-$ and $^{\bullet}OH$ under visible light illumination because of their wide band gap. Therefore, a Z-Scheme model was proposed to interpretate the reaction mechanism[40]. As portrayed in scheme 1, the existence of Sn vacancies in Zn_2SnO_4 (as confirmed by XPS and EPR results) renders the formation of some new defect levels in SnO_2 and Zn_2SnO_4, which results in the reduced bandgaps of SnO_2 and Zn_2SnO_4. The Sn vacancies and the accompanying the introduction of graphene expand the light absorption from UV to visible light region. Then, the photo-produced electrons in the CB of SnO_2 can migrate to the VB of Zn_2SnO_4, which can further be excited to the CB of Zn_2SnO_4. Origining from the strong affinity of electrons to graphene, the photo-generated electrons in the CB of Zn_2SnO_4 can easily transfer to graphene, which are then captured by oxygen, producing $^{\bullet}O_2^-$. While holes are leaving behind in the VB of SnO_2, which are powerful to oxidize surface adsorbed OH^-/H_2O into $^{\bullet}OH$ radicals (2.4 V *versus* NHE). ESR analysis confirms the production of $^{\bullet}O_2^-$ and $^{\bullet}OH$ radicals, which are main ROSs that involves in the oxidation of NO and acetone (eqs. 5-9).

3.10 Photochemical stability.

From the viewpoint of practical applications, the stability of the catalysts is of great importance[44]. Therefore, we evaluated the stability of SnO_2-Zn_2SnO_4/graphene photocatalyst (ZL-G3 as an example) in photocatalytical removal of NO for several runs (Fig. 13). Significantly, the photocatalyst still keeps high photocatalytic performance even after consecutive five cycles without a slight decrease in photocatalytic activity, which demonstrates that the robust stability of the surface vacancies-rich nanocomposite. Such eminent graphene-assisted Z-scheme SnO_2-Zn_2SnO_4 heterostructure with high photocatalytic capability and excellent stability makes it promising to be widely used in purification of polluted gas in a scale-up.

4. Conclusions

In summary, for the first time, visible-light-responsive photocatalyst SnO_2-Zn_2SnO_4/graphene was successfully fabricated by a facile one-pot hydrothermal reaction strategy. The presence of graphene not only cause the production of SnO_2 but also results in the formation of Sn vacancies, which makes it responsive to visible light. A Z-scheme model was proposed for the photocatalytic oxidation of NO and acetone over SnO_2-Zn_2SnO_4/graphene hybridized photocatalyst, and both $^{\bullet}O_2^-$ and $^{\bullet}OH$ radicals are identified to be the main ROSs that should be responsible for the oxidation of NO and acetone. When compared with normal Zn_2SnO_4 which was prepared in the absence of graphene, Z-scheme SnO_2-Zn_2SnO_4 heterostructures with vacancies obviously display much higher photocatalytic activity because of the enlarged BET specific surface area, improved light-harvesting ability and promoted separation of photo-generated carriers.

Acknowledgements

This research was financially supported by the National Key Research and Development Program of China (2016YFA0203000), the National Natural Science Foundation of China (51672312 & 21373275) and the Science and Technology Program of Wuhan, China (2016010101010018 & 2015070504020220).

References:

[1] F. Dong, Z.W. Zhao, Y.J. Sun, Y.X. Zhang, S. Yan, Z.B. Wu, An advanced semimetal-organic Bi spheres-g-C_3N_4 nanohybrid with SPR-enhanced visible-light photocatalytic performance for NO purification, Environ. Sci. Technol. 49 (2015) 12432-12440.

[2] Z.H. Ai, W.K. Ho, S.C. Lee, L.Z. Zhang, Efficient photocatalytic removal of NO in indoor air with hierarchical bismuth oxybromide nanoplate microspheres under visible light, Environ. Sci. Technol. 43 (2009) 4143-4150.

[3] K.L. Lv, Q.J. Xiang, J.G. Yu, Effect of calcination temperature on morphology and photocatalytic activity of anatase TiO_2 nanosheets with exposed {001} facets, Appl. Catal. B 104 (2011) 275-281.

[4] Y.H. Li, W.K. Ho, K.L. Lv, B.C. Zhu, S.C. Lee, Carbon vacancy-induced enhancement of the visible light-driven photocatalytic oxidation of NO over g-C_3N_4 nanosheets, Appl. Surf. Sci. (2017) https://doi.org/10.1016/j.apsusc.2017.06.054.

[5] A.L. Linsebigler, G.Q. Lu, J.T. Yates,Photocatalysis on TiO_2 surfaces: principles, mechanisms, and selected results, Chem. Rev. 95 (1995) 735-758.

[6] R. Asahi, T. Morikawa, T. Ohwaki, K. Aoki, Y. Taga, Visible-light photocatalysis in nitrogen-doped titanium oxides, Science 293 (2001) 269-271.

[7] Y.M. He, L.H. Zhang, B.T. Teng, M.H. Fan, A new application of Z-scheme Ag_3PO_4/g-C_3N_4 composite in converting CO_2 to fuel, Environ. Sci. Technol. 49 (2015) 649-656.

[8] R.W. Yang, J.H. Cai, K.L. Lv, X.F. Wu, W.G. Wang, Z.H. Xu, M. Li, Q. Li, W.Q. Xu, Fabrication of TiO_2 hollow microspheres assembly from nanosheets (TiO_2-HMSs-NSs) with enhanced photoelectric conversion efficiency in DSSCs and photocatalytic activity, Appl. Catal. B 210 (2017) 184-193.

[9] M.A. Alpuche-Aviles, Y. Wu, Photoelectrochemical study of the band structure of Zn_2SnO_4 prepared by the hydrothermal method, J. Am. Chem. Soc. 131 (2009) 3216-3224.

[10] C.G. Anchieta, D. Sallet, E.L. Foletto, S.S. da Silva, O. Chiavone-Filho, C.A.O. do Nascimento, Synthesis of ternary zinc spinel oxides and their application in the photodegradation of organic pollutant, Ceram. Int. 40 (2014) 4173-4178.

[11] J.H. Wang, H. Li, S.G. Meng, L. Zhang, X.L. Fu, S.F. Chen, One-pot hydrothermal synthesis of highly efficient SnO_x/Zn_2SnO_4 composite photocatalyst for the degradation of methyl orange and gaseous benzene, Appl. Catal. B 200 (2017) 19-30.

[12] B. Li, E.Y. Guo, C.X. Wang, L.W. Yin, Novel Au inlaid Zn_2SnO_4/SnO_2 hollow rounded cubes for dye-sensitized solar cells with enhanced photoelectric conversion performance, J. Mater. Chem. A 4 (2016) 466-477.

[13] Q. Zhu, Y. Peng, L. Lin, C.M. Fan, G.Q. Gao, R.X. Wang, A.W. Xu, Stable blue TiO_{2-x} nanoparticles for efficient visible light photocatalysts J. Mater. Chem. A 2 (2014) 4429-4437.

[14] A.W. Xu, Y. Gao, H.Q. Liu, The preparation, characterization, and their photocatalytic activities of rare-earth-doped TiO_2 nanoparticles, J. Catal. 207 (2002) 151-157.

[15] H.L. Guo, Q. Zhu, X.L. Wu, Y.F. Jiang, X. Xie, A.H. Xu, Oxygen deficient ZnO_{1-x} nanosheets with high visible light photocatalytic activity, Nanoscale 7 (2015) 7216-7223.

[16] C.H. Liang, Y. Shimizu, T. Sasaki, N. Koshizaki, Synthesis of ultrafine SnO_{2-x} nanocrystals by pulsed laser-induced reactive quenching in liquid medium, J. Phys. Chem. B 107 (2003) 9220-9225.

[17] Y. Xia, Q. Li, K.L. Lv, D.G. Tang, M. Li, Superiority of graphene over carbon analogs for enhanced photocatalytic H2-production activity of $ZnIn_2S_4$, Appl. Catal. B 206 (2017) 344-352.

[18] X.F. Wu, L.L. Wen, K.L. Lv, K.J. Deng, D.G. Tang, H.P. Ye, D.Y. Du, S.N. Liu, M. Li, Fabrication of ZnO/graphene flake-like photocatalyst with enhanced photoreactivity, Appl. Surf. Sci. 358 (2015) 130-136.

[19] Q.J. Xiang, J.G. Yu, M. Jaroniec, Graphene-based semiconductor photocatalysts, Chem. Soc. Rev. 41 (2012) 782-796.

[20] F. Li , P.H. Du, W. Liu, X.S. Li, H.D. Ji, J. Duan, D.Y. Zhao, Hydrothermal synthesis of graphene grafted titania/titanate nanosheets for photocatalytic degradation of 4-chlorophenol: Solar-light-driven photocatalytic activity and computational chemistry analysis, Chem. Eng. J. 331 (2018) 685-694.

[21] S.Y. Dong, X.H. Ding, T. Guo, X.P. Yue, X. Han, J.H. Sun, Self-assembled hollow sphere shaped Bi_2WO_6/RGO composites for efficient sunlight-driven photocatalytic degradation of organic pollutants, Chem. Eng. J. 316 (2017) 778-789.

[22] W.K. Jo, N.C.S. Selvam, Z-scheme CdS/g-C_3N_4 composites with RGO as an electron mediator for efficient photocatalytic H_2 production and pollutant degradation, Chem. Eng. J. 317 (2017) 913-924.

[23] Z.G. Lu, Y.G. Tang, Two-step synthesis and ethanol sensing properties of Zn_2SnO_4/SnO_2 nanocomposites, Mater. Chem. Phys. 92 (2005) 5-9.

[24] Z.Z. Dong, D. Huo, B.H. Kear, S.D. Tse, Combined flame and solution synthesis of nanoscale tungsten-oxide and zinc/tin-oxide heterostructures, Nanoscale 7 (2015) 20510-20520.

[25] A.A. Firooz, A.R. Mahjoub, A.A. Khodadadi, M. Movahedi, High photocatalytic activity of Zn_2SnO_4 among various nanostructures of $Zn_{2x}Sn_{1-x}O_2$ prepared by a

hydrothermal method, Chem. Eng. J. 165 (2010) 735-739.

[26] M. Miyauchi, Z.F. Liu, Z.G. Zhao, S. Anandan, K. Hara, Single crystalline zinc stannate nanoparticles for efficient photo-electrochemical devices, Chem. Commun. 46 (2010) 1529-1531.

[27] P. Junploy, S. Thongtem, T. Thongtem, A. Phuruangrat, Photocatalytic activity of Zn_2SnO_4-SnO_2 nanocomposites produced by sonochemistry in combination with high temperature calcinations, Superlatt. Microstruct. 74 (2014) 173-183.

[28] J.Z. Yin, F. Gao, C.Z. Wei, Q.Y. Lu, Controlled growth and applications of complex metal oxide $ZnSn(OH)_6$ Polyhedra, Inorg. Chem. 51 (2012) 10990-10995.

[29] G. Sun, S.S. Zhang, Y.W. Li, Solvothermal synthesis of Zn_2SnO_4 nanocrystals and their photocatalytic properties, Int. J. Photoenergy 2014 (2014) 580615-580622.

[30] M. Chitra, K. Uthayaranil, N. Rajasekaran, N. Neelakandeswari, E.K. Girija, D. Pathinettam, $ZnO/SnO_2/Zn_2SnO_4$ nanocomposite: preparation and characterization for gas sensing applications, Padiya Nanosystems: Phys. Chem. Math. 7 (2016) 707-710.

[31] J.P.C. Baena, D. A. Kriz, M. Giotto, S. L. Suib, A. G. Agrios, Fluoride additive in epoxide-initiated sol-gel synthesis enables thin-film applications of SnO_2 aerogels, RSC Adv. 26 (2016) 21326-21331.

[32] E.M. Golden, S.A. Basun, D.R. Evans, A.A. Grabar, I.M. Stoika, N.C. Giles, L.E. Halliburton, Sn vacancies in photorefractive $Sn_2P_2S_6$ crystals: An electron paramagnetic resonance study of an optically active hole trap, J. Appl. Phys. 120 (2016) 133101.

[33] V. Georgakilas, J. N. Tiwari, K.C. Kemp, J. A. Perman, A. B. Bourlinos, K. S. Kim, R. Zboril, Noncovalent functionalization of graphene and graphene oxide for energy materials, biosensing, catalytic, and biomedical applications, Chem. Rev. 116 (2016) 5464-5519.

[34] Y.H. Zhang, N. Zhang, Z.R. Tang, Y.J. Xu, Graphene transforms wide band gap ZnS to a visible light photocatalyst: the new role of graphene as a macromolecular photosensitizer, ACS Nano 6 (2012) 9777-9789.

[35] Y.J. Sun, W.D. Zhang, T. Xiong, Z.W. Zhao, F. Dong, R.Q. Wang, W.K. Ho, Growth of BiOBr nanosheets on C3N4 nanosheets to construct two-dimensional nanojunctions with enhanced photoreactivity for NO removal, J. Colloid Interf. Sci. 418 (2014) 317-323.

[36] F. Dong, Y.J. Sun, M. Fu, Z.B. Wu, S.C. Lee, Room temperature synthesis and highly enhanced visible light photocatalytic activity of porous BiOI/BiOCl composites nanoplates microflowers, J. Hazard. Mater. S219-220 (2012) 26-36.

[37]Y.H. Li, K.L. Lv, W.K. Ho, Z.W. Zhao, H. Yu, Enhanced visible-light photo-oxidation of nitric oxide using bismuth-coupled graphitic carbon nitride composite heterostructures, Chin. J. Catal. 38 (2017) 321-329.

[38] Y.N. Cho, Y.D. Choi, Graphene oxide-photosensitizer conjugate as a redox-responsive theranostic agent, Chem. Commun. 48 (2012) 9912-9914.

[39] T. Xiong, F. Dong, Z.B. Wu, Enhanced extrinsic absorption promotes the visible light photocatalytic activity of wide band-gap $(BiO)_2CO_3$ hierarchical structure, RSC Adv. 4 (2014) 56307-56312.

[40] Y.H. Li, K.L. Lv, W.K. Ho, F. Dong, X.F. Wu, Y. Xia, Hybridization of rutile TiO_2 ($rTiO_2$) with g-C_3N_4 quantum dots (CN QDs): an efficient visible-light-driven Z-scheme hybridized photocatalyst, Appl. Catal B: Environ. 202 (2017) 611-619.

[41] W.D. Zhang, F. Dong, W. Zhang, Capture of atmospheric CO_2 into $(BiO)_2CO_3$/graphene or grapheneoxide nanocomposites with enhanced photocatalytic performance, Appl. Surf. Sci. 358 (2015) 75-83.

[42] F. Dong, Z.Y. Wang, Y.H. Li, W.K. Ho, S.C. Lee, Immobilization of polymeric

g-C_3N_4 on structured ceramic foam for efficient visible light photocatalytic air purification with real indoor illumination, Environ. Sci. Technol. 48 (2014) 10345-10353.

[43] R. Beranek, Adv. Phys. Chem. 2011 (2011) 786759.

[44] H. Yang, K.L. Lv, J.J. Zhu, Q. Li, D.G. Tang, W.K. Ho, M. Li, S.A.C. Carabineiro, Effect of mesoporous g-C_3N_4 substrate on catalytic oxidation of CO over Co_3O_4, Appl. Surf. Sci. 401 (2017) 333-340.

Table 1. Physical property and photocatalytic activity of the photocatalyst.

Sample	S_{BET} (m^2g^{-1})	Pore volume (cm^3g^{-1})	Peak diameter (nm)	η_{NO}[a] (%)	Degraded acetone (ppm)
ZL	21.3	0.05	3.47/5.06	11.8	13.9
ZL-G1	22.0	0.05	3.43/4.62	41.5	30.00
ZL-G3	23.7	0.04	3.45/5.01	59.3	33.5
ZL-G5	24.3	0.05	3.47/5.10	32.6	30.0

[a] Removal efficiency of NO.

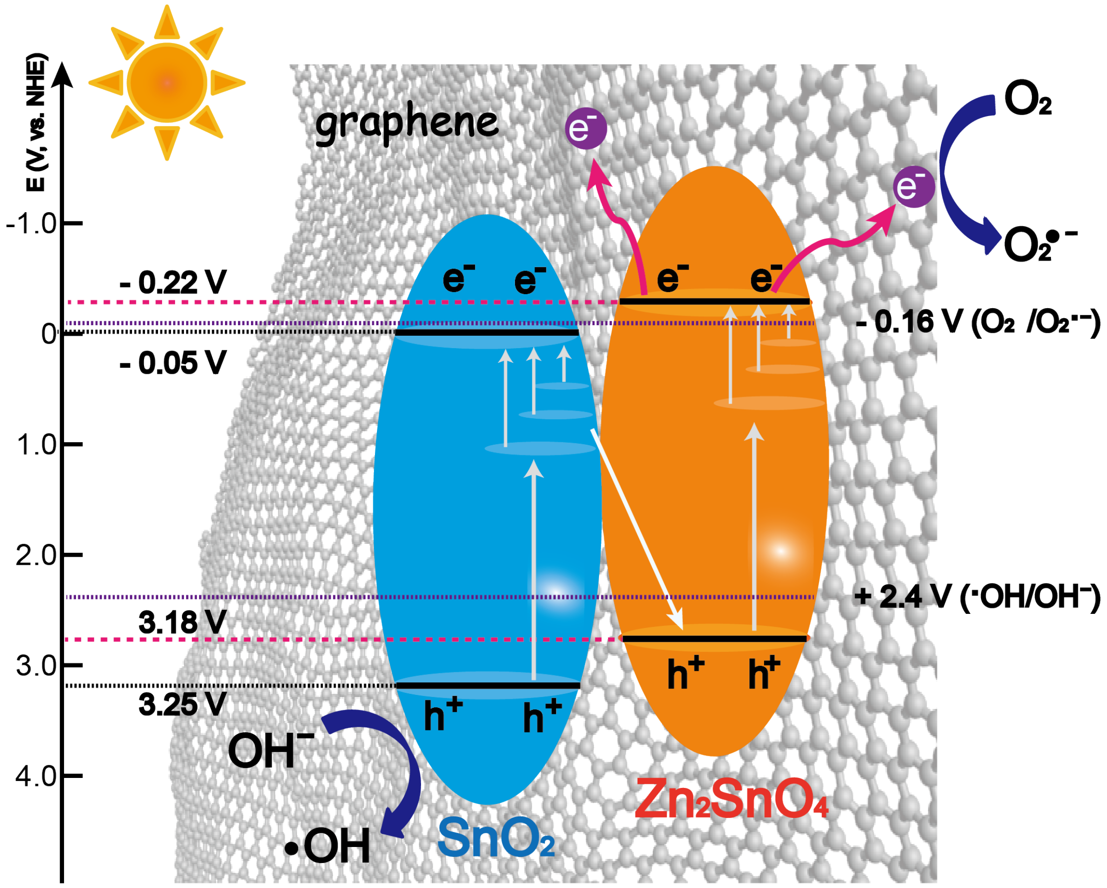

Scheme 1. Proposed *Z*-scheme mechanism for the visible-light-driven photocatalytic reaction of the three-component-photocatalyst (SnO_2/Zn_2SnO_4/graphene).

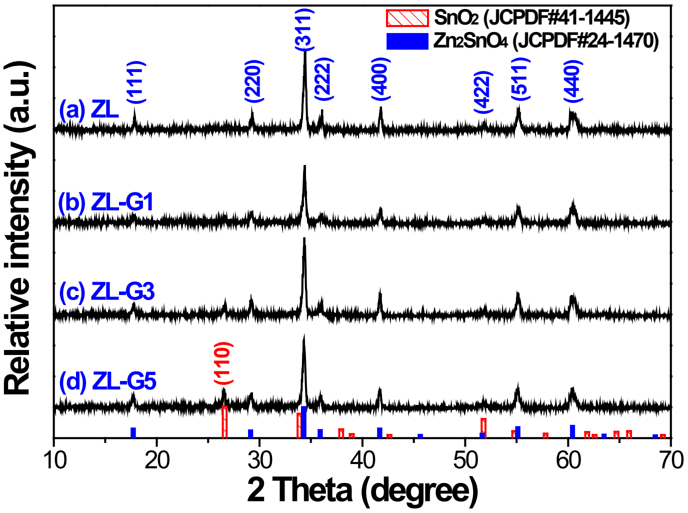

Fig. 1. XRD patterns of the as-synthesized photocatalysts, together with the expected diffraction peaks for Zn_2SnO_4 and SnO_2, respectively.

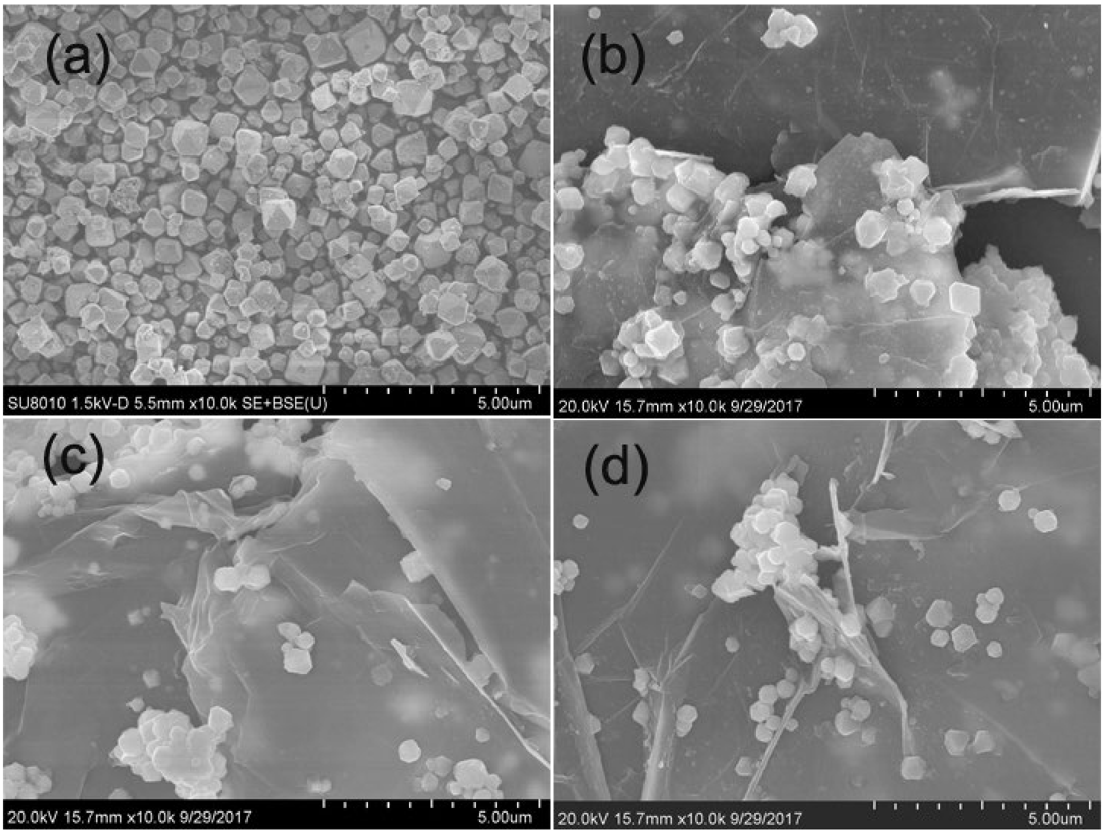

Fig. 2. SEM images of ZL (a), ZL-G1 (b), ZL-G3 (c) and ZL-G5 (d) photocatalysts.

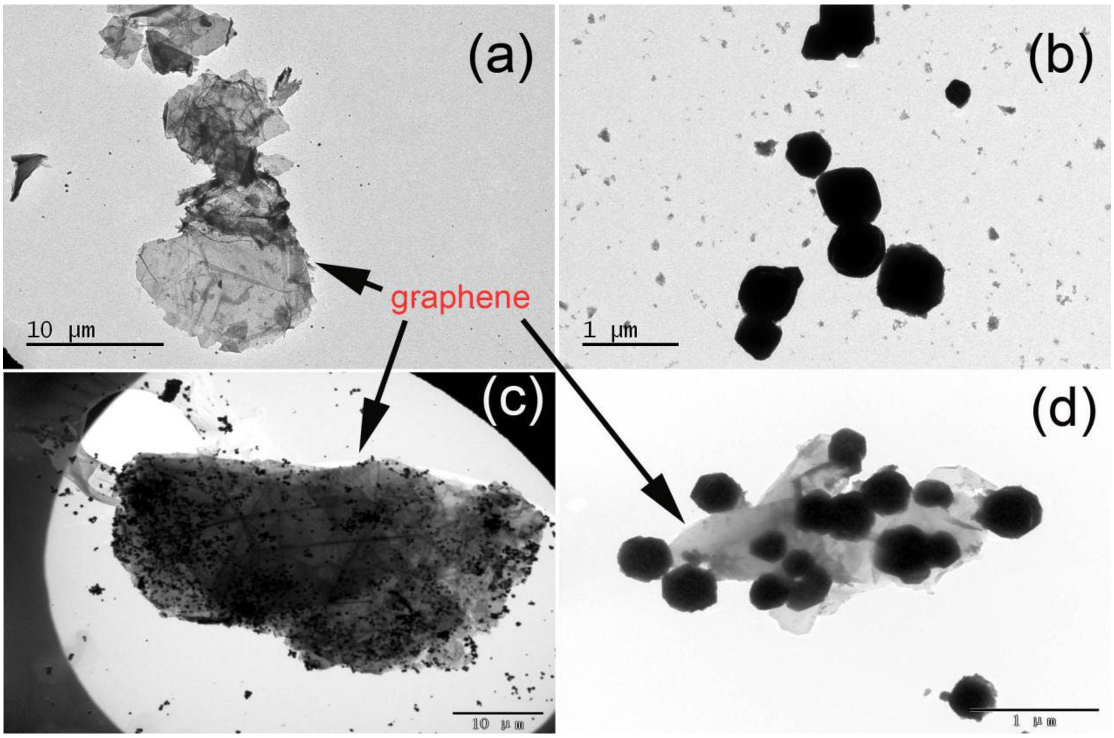

Fig. 3. TEM images of graphene (a), ZL (b), and the optimized ZL-G3 (c) samples. Arrows indicate the presence of graphene.

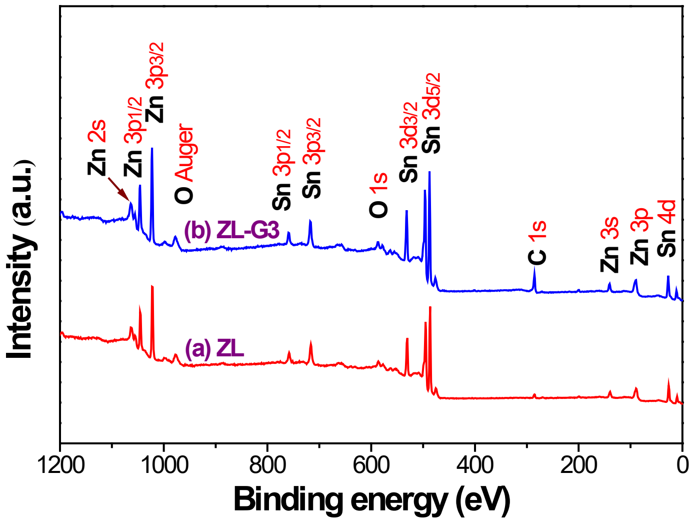

Fig. 4. Representative survey XPS spectra of Zn_2SnO_4 samples before (a, ZL) and after modified by graphene (b, ZL-G3).

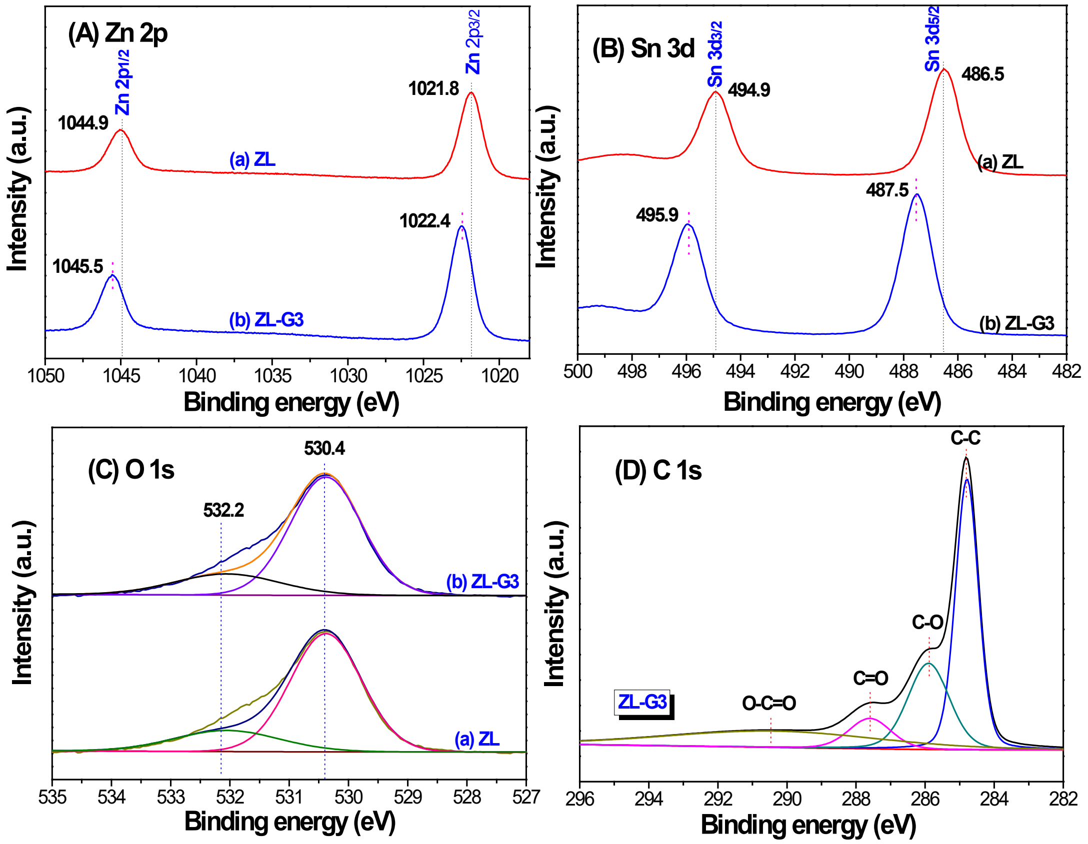

Fig. 5. High resolution XPS spectra of the photocatalysts in regions of Zn 2p (A), Sn 3d (B), O 1s (C) and C 1s (D).

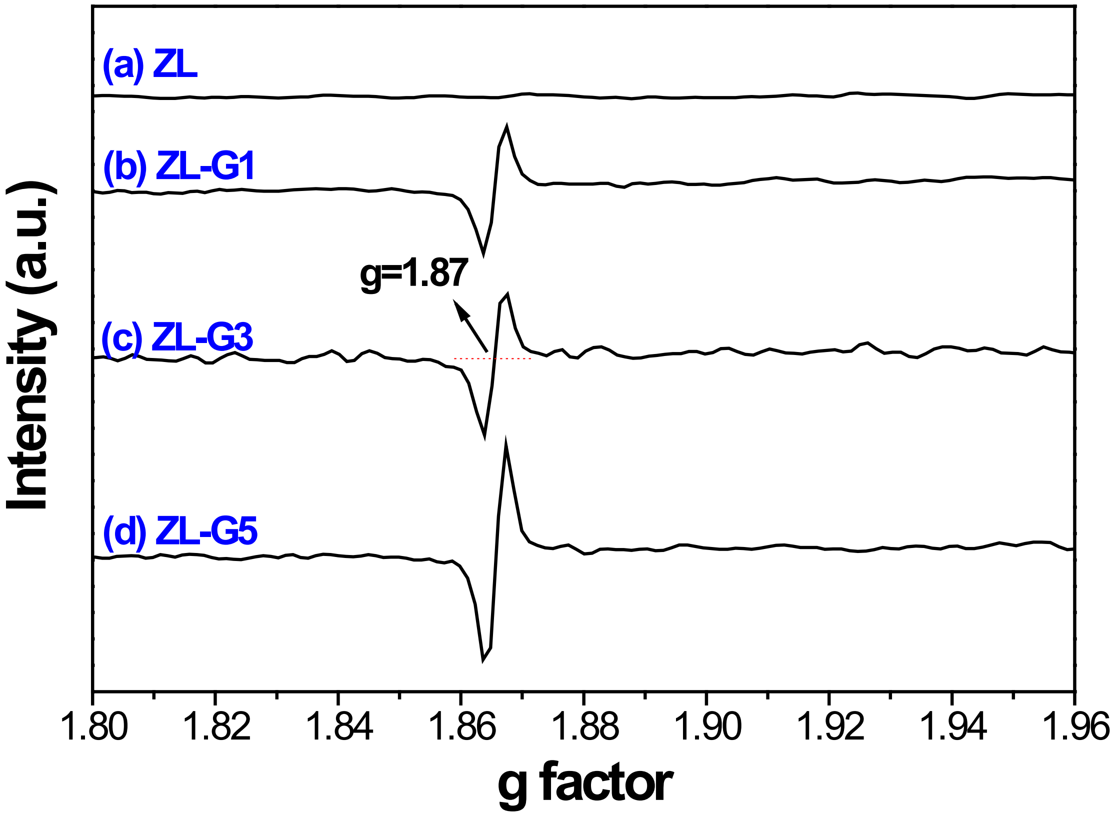

Fig. 6. Comparison of the EPR of the photocatalysts.

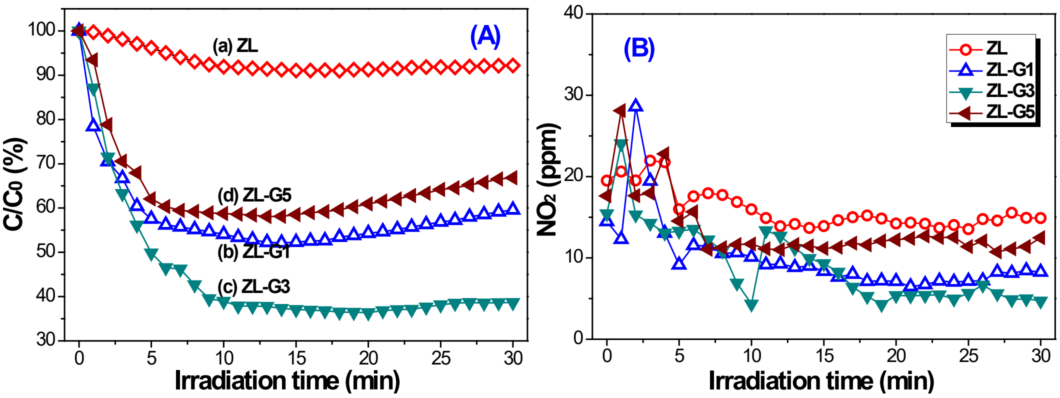

Fig. 7. Photocatalytic oxidation profiles of NO (A) and the production of NO_2 (B).

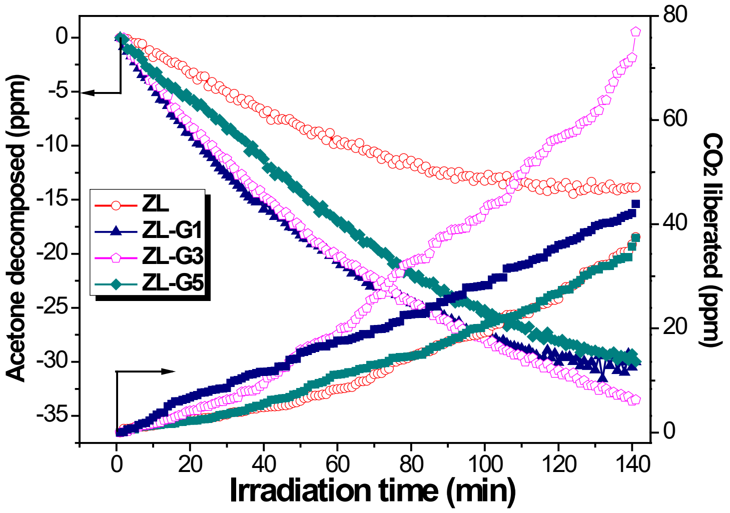

Fig. 8. The dependence of the degraded acetone and released CO_2 (ppm) on irradiation time.

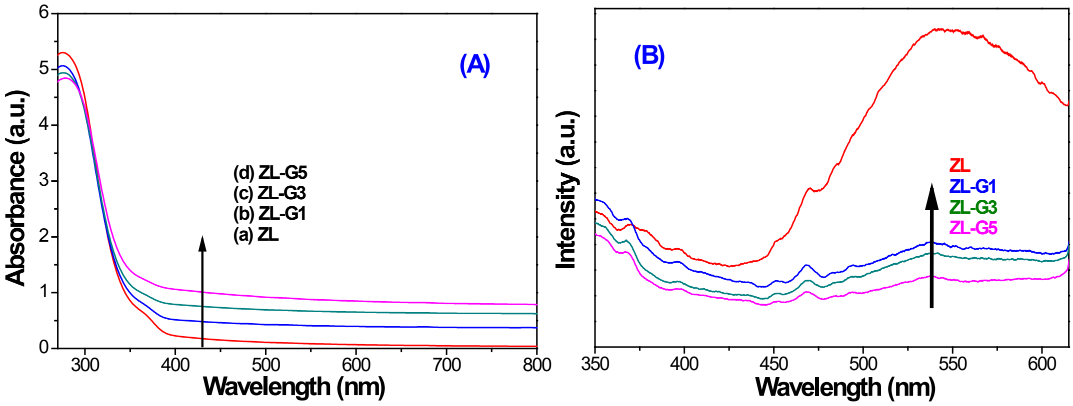

Fig. 9. UV-vis DRS (A) and PL spectra (B) of the as-synthesized photocatalysts (315 nm emission).

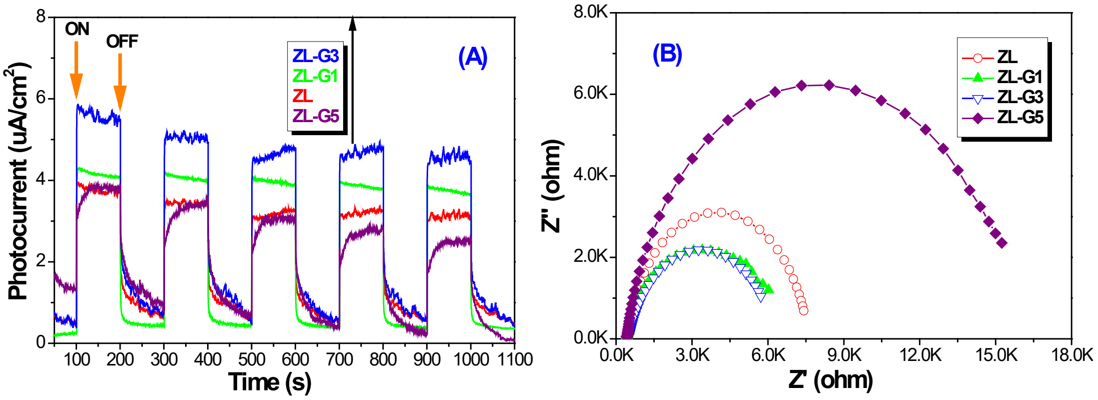

Fig. 10. Transient photocurrent responses (A) and electrochemical impedance spectroscopy (EIS) Nynquist plots (B) of the photocatalysts.

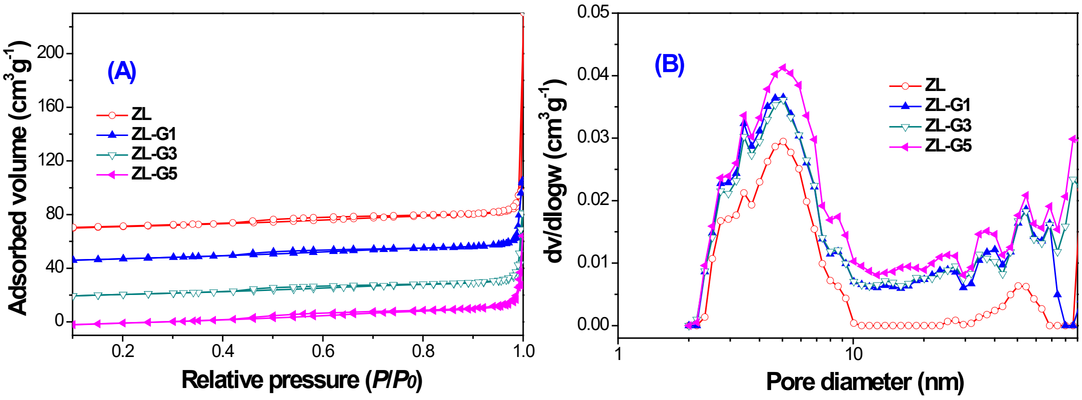

Fig. 11. Nitrogen adsorption-desorption isotherms (A) and the corresponding pore-size distribution curves (B) of the photocatalysts.

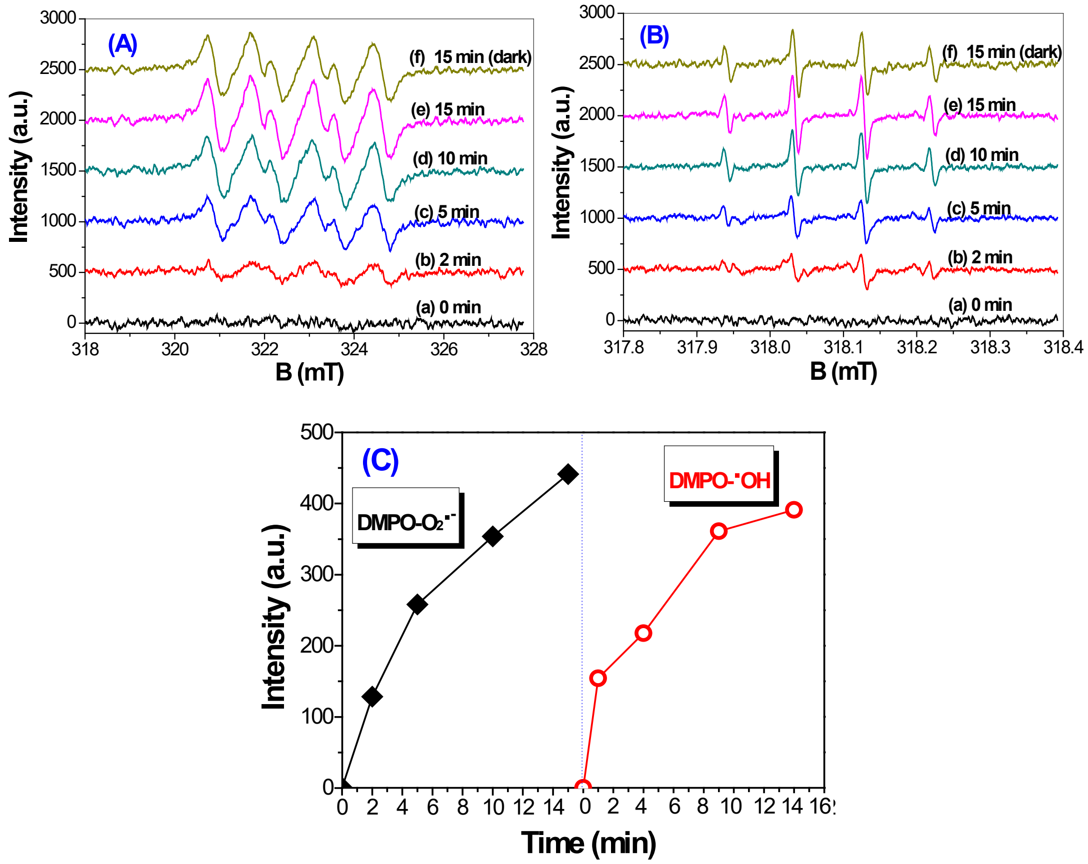

Fig. 12. ESR signals of DMPO-$O_2\cdot^-$ (A) and DMPO-·OH (B) adducts of ZL-G3 photocatalyst, together with the signal intensity changes as a function of time (C) under visible light illumination (λ>400 nm).

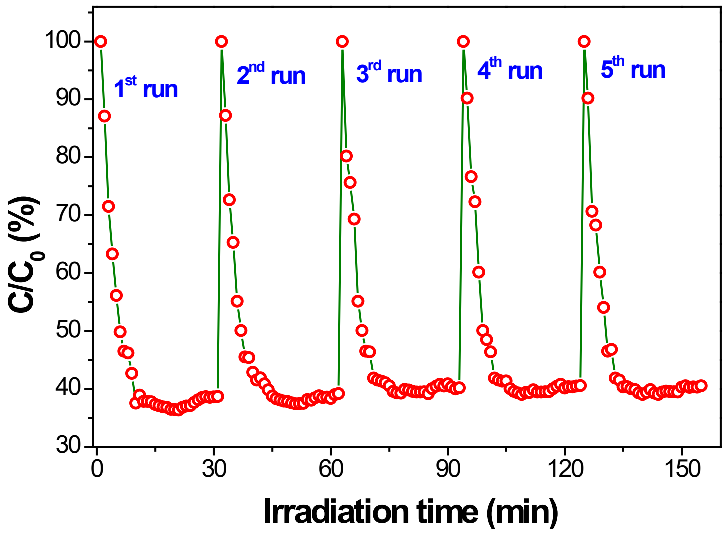

Fig. 13. Five consecutively cycling runs for the photocatalytic oxidation of NO over ZL-G3 sample under visible light irradiation.